

Supporting Information

Droplet Self-Propulsion on Superhydrophobic Microtracks

*Christos Stamatopoulos,^{†,||,¶} Athanasios Milionis,^{‡,||} Norbert Ackerl,^{§,||} Matteo Donati,[‡] Paul
Leudet de la Vallée,[‡] Philipp Rudolf von Rohr,^{†,*} Dimos Poulikakos^{‡,*}*

[†]Transport Processes and Reactions Laboratory, [‡]Laboratory of Thermodynamics in Emerging Technologies, and [§] Institute of Machine Tools and Manufacturing, Department of Mechanical and Process Engineering, ETH Zurich, Zurich, Switzerland.

[¶]Present address: High Voltage Laboratory, Department of Information Technology and Electrical Engineering, ETH Zurich, Zurich, Switzerland.

^{||}Denotes equal contribution.

*E-mail: dpoulikakos@ethz.ch; vonrohr@ipe.mavt.ethz.ch

Discussion S1: Derivation of net propulsion force F_n calculation.

The shape of the menisci between tracks under the droplet depends on the water contact angle at the edges of the microgrooves (see Figure S1). We assume that this contact angle is between advancing θ_{adv} and receding θ_{rec} contact angles on a planar superhydrophobic surface with an identical nanoneedle surface structure. Therefore, to assist and simplify our calculations of the net propulsion force F_n we are going to use $\theta = (\theta_{adv} + \theta_{rec})/2 = 163.3^\circ$. The component of the surface tension, or adhesion force per unit length, σ_{xy} , is normal to the top edge of the microgrooves. For the calculation of the radius of curvature of the meniscus at a position x from the beginning of the microtracks we consider a cut $A' - A'$ in such a way so that it is normal to the axis as shown in Figure S1a(i). Due to the fact that the ridge edges are not parallel, note the difference between the half-width normal to the microgroove edge, $w'/2$, compared to the half-width normal to the centerline, as shown in Fig S1. These are related as:

$$w = w' \cdot \cos \frac{\alpha}{2}. \quad (S1)$$

Since we examine opening angles $\alpha \leq 9^\circ$ then we can safely assume with negligible error that $\cos \frac{\alpha}{2} \approx 1$ which leads to the assumption $w' \approx w$, and simplifies significantly the analysis (see Figure S1a(ii)). This is shown in a magnified view in Figure S1a(ii). For the same reason, for the shape analysis of the meniscus, we can assume that σ and its components σ_z and σ_{xy} reside at the same plane, which is normal to the channel centerline and that $\sigma_{xy} \approx \sigma_y$ (Figure S1b). With the help of Figure S1 the width w at a position x is given by the following equation:

$$w(x) = 2 \tan \frac{\alpha}{2} \cdot x + w_0, \quad (S2)$$

where w_0 corresponds to the start of the channel (Figure S1a(i)). In addition, from Figure S1b the radius of curvature $R(x)$ of the meniscus is given by the equation

$$R(x) = \frac{w(x)}{2 \sin \psi}, \quad (S3)$$

where $\psi = \theta - \varepsilon - \pi/2$.

Combining equations S2 and S3 we obtain an expression of $R(x)$

$$R(x) = \frac{2 \tan \frac{\alpha}{2} \cdot x + w_0}{2 \sin \psi} . \quad (\text{S4})$$

Therefore, the pressure difference outside, P_{out} to inside, P_{in} , of the meniscus at the position x is given by the Young-Laplace equation:¹

$$\Delta P_L(x) = P_{\text{in}}(x) - P_{\text{out}} = \frac{\sigma}{R(x)} . \quad (\text{S5})$$

Combining equations S4 and S5 we obtain

$$P_{\text{in}}(x) = \frac{2\sigma \sin \psi}{2 \tan \frac{\alpha}{2} \cdot x + w_0} + P_{\text{out}} . \quad (\text{S6})$$

Taking into consideration equation S4 and Figure S1b we can derive the meniscus shape, which is part of a truncated cone of height $l(x)$ and it is shown in Figure S1c(i). Again, in order to simplify the analysis, since we are examining surfaces with $\alpha \leq 9^\circ$, the radius of curvature of the meniscus free surface can be approximated with the corresponding radius of the truncated cone cross section, as shown in Figure S1c(i) introducing a negligible maximum deviation of 0.34%. Therefore, the infinitesimal volume $d\Omega''$ of the meniscus is given by the following equation:

$$d\Omega'' = A_m(x) dx , \quad (\text{S7})$$

where $A_m(x)$ is the surface area of the cross section of the meniscus (Figure S1c(ii)). The surface area $A_m(x)$ can be calculated by the following equation (Figure S1c(ii)):

$$A_m(x) = A_s(x) - A_t(x) , \quad (\text{S8})$$

where $A_s(x)$ is the surface area of the sector formed by the minor arc $\widehat{\text{BD}}$ and the center of the circle O (Figure S1c(ii)) and $A_t(x)$ is the surface area of the triangle $\triangle \text{OBD}$. Therefore:

$$A_s(x) = \psi R^2(x) \quad \text{and} \quad (\text{S9})$$

$$A_t(x) = R^2(x) \cos \psi \sin \psi . \quad (\text{S10})$$

Combining equations S8, S9 and S10 we obtain the expression of $A_m(x)$ which is

$$A_m(x) = R^2(x)(\psi - \cos \psi \sin \psi) . \quad (\text{S11})$$

Based on equations S7 and S11 $d\Omega''$ is given by the following equation:

$$d\Omega'' = R^2(x)(\psi - \cos\psi \sin\psi)dx . \quad (S12)$$

The propulsion force F_p exerted on the meniscus, is estimated by integrating the pressure gradient ∇P_{in} over the volume of the meniscus Ω' :^{2,3}

$$F_p = -\iiint_{\Omega'} \nabla P_{in} \cdot d\Omega'' . \quad (S13)$$

Based on equation S6, the pressure gradient ∇P_{in} can be approximated with the derivative of P_{in} with respect to x :

$$\nabla P_{in} = \frac{dP_{in}}{dx} = -\frac{4 \cdot \sigma \cdot \tan \frac{\alpha}{2} \cdot \sin \psi}{(2 \tan \frac{\alpha}{2} \cdot x + w_0)^2} . \quad (S14)$$

Moreover, combining equation S4 and S12 we obtain:

$$d\Omega'' = \frac{(2 \tan \frac{\alpha}{2} \cdot x + w_0)^2}{4 \sin^2 \psi} (\psi - \cos\psi \sin\psi) dx . \quad (S15)$$

With the help of equations S14 and S15, equation S13 becomes:

$$F_p = \int_{x_r}^{x_f} \sigma \tan \frac{\alpha}{2} \frac{\psi - \cos\psi \sin\psi}{\sin\psi} dx \quad (S16)$$

which leads to the final expression of F_p :

$$F_p = \sigma \cdot l(x) \cdot \tan \frac{\alpha}{2} \frac{\psi - \cos\psi \sin\psi}{\sin\psi} . \quad (S17)$$

Since $\alpha \leq 9^\circ$ then $\tan \frac{\alpha}{2} \approx \frac{\alpha}{2}$ simplifying equation S17 to the following form:

$$F_p = \sigma \cdot l \cdot a \cdot \kappa_p , \quad (S18)$$

where $\kappa_p = \frac{\psi - \cos\psi \sin\psi}{2 \sin\psi}$.

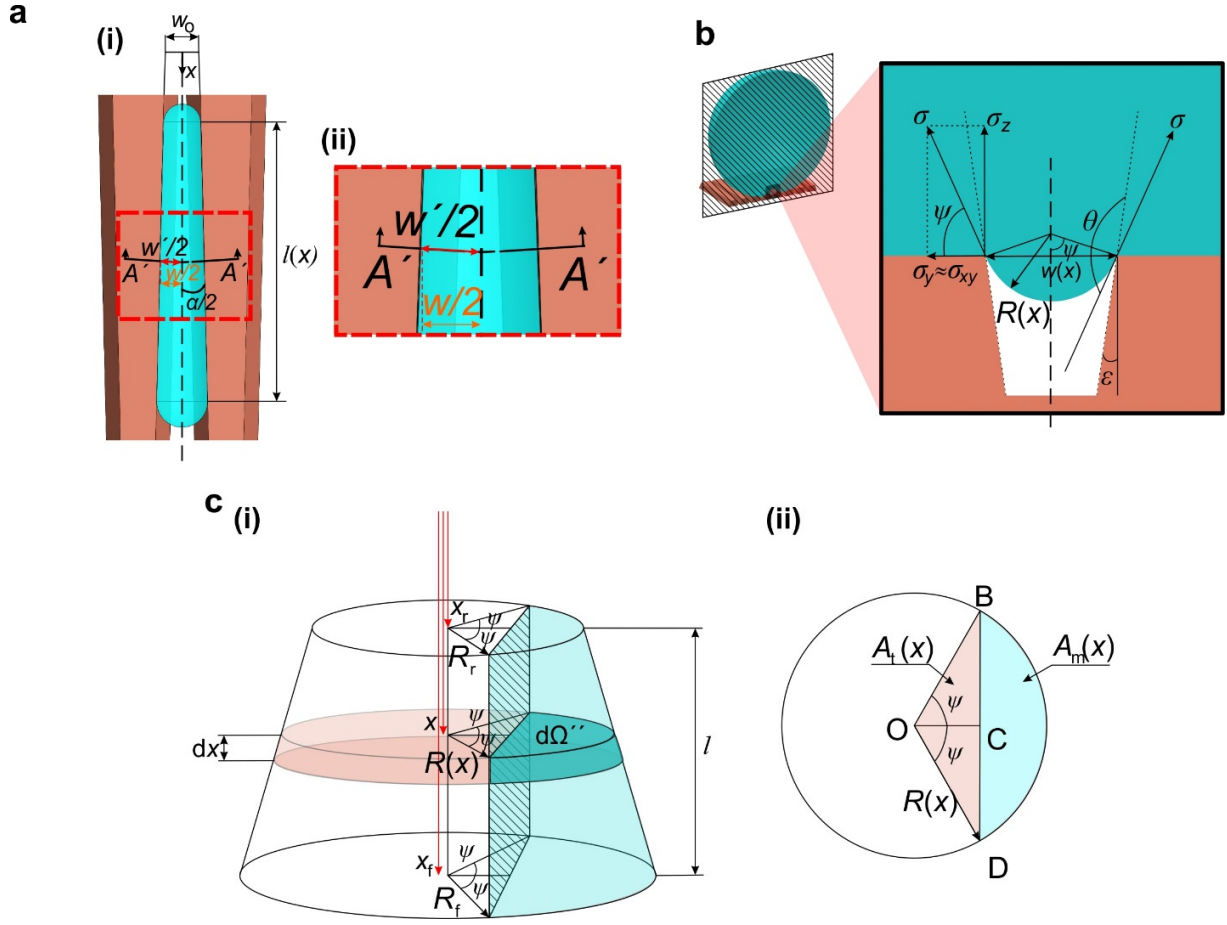


Figure S1. (a) (i) Simplification of the analysis by approximating w to w' (ii) Magnification of the cut $A' - A'$ (b) Geometrical considerations about the meniscus' cross section due to cut $A' - A'$. (c) Shape of the meniscus and associated geometrical considerations. (i) The meniscus is part of a truncated cone (teal color). (ii) Cross section of the truncated cone at position x .

The adhesion force, F_a , also needs to be estimated (Figure S2a). This is done by integrating σ_x over the length S of the two microgroove edges with which the meniscus is in contact (Figure S2b)

$$F_a = 2 \cdot \kappa_\phi \cdot \int_S \sigma_x \cdot dS' \quad (\text{S19})$$

where κ_ϕ is the fraction of the length of the microgroove top edge that is actually in contact with the meniscus through the tips of the nanoroughness.⁴

According to the definitions of Figure S2a,

$$\sigma_{xy} = \sigma \cdot \cos \psi , \quad (\text{S20})$$

$$\sigma_x = \sigma_{xy} \cdot \sin \frac{\alpha}{2} . \quad (\text{S21})$$

Hence,

$$\sigma_x = \sigma \cdot \cos \psi \cdot \sin \frac{\alpha}{2} . \quad (\text{S22})$$

Combining equations S19 and S22 we obtain:

$$F_a = 2 \cdot \kappa_\varphi \cdot \int_S \sigma \cdot \cos \psi \cdot \sin \frac{\alpha}{2} \cdot dS' . \quad (\text{S23})$$

Since $dS' = \frac{dx}{\cos \frac{\alpha}{2}}$ equation S23 becomes:

$$F_a = 2 \cdot \kappa_\varphi \cdot \sigma \cdot \cos \psi \cdot \tan \frac{\alpha}{2} \int_l dx = \sigma \cdot l \cdot \alpha \cdot \cos \psi \cdot \kappa_\varphi . \quad (\text{S24})$$

To simplify the estimation of the κ_φ we assume that the nanoneedles of the nanoroughness have a circular cross section of radius R_n and are forming an array with pitch p_n (Figure S2c). The fraction φ of the surface area in contact with water⁵ for the control volume, the top view of which is shown in Figure S2c with black translucent square, is given by the following equation:

$$\varphi = \frac{9 \cdot \pi \cdot R_n^2}{9 \cdot p_n^2} = \frac{\pi \cdot R_n^2}{p_n^2} . \quad (\text{S25})$$

Also, at the sides of the cross section of the control volume the fraction of the length of each side of the square surface in contact with the liquid is:

$$\kappa_\varphi = \frac{6 \cdot R_n}{3 \cdot p_n} = \frac{2 \cdot R_n}{p_n} . \quad (\text{S26})$$

Combining S26 and S25:

$$\kappa_\varphi = 2 \frac{\varphi^{1/2}}{\pi^{1/2}} . \quad (\text{S27})$$

With the help of equations S24 and S27, F_a reads:

$$F_a = \sigma \cdot l \cdot \alpha \cdot \cos \psi \cdot 2 \frac{\varphi^{1/2}}{\pi^{1/2}} = \sigma \cdot l \cdot \alpha \cdot \kappa_a. \quad (\text{S28})$$

where $\kappa_a = 2 \cdot \cos \psi \cdot \frac{\varphi^{1/2}}{\pi^{1/2}}$.

To estimate φ we use the equation for the Cassie-Baxter state:^{5,6}

$$\cos \theta = -1 + \varphi(\cos \theta_E + 1) \quad (\text{S29})$$

where θ_E is the static contact angle of water on a smooth copper surface coated with perfluorodecanethiol.

From equation S29:

$$\varphi = \frac{\cos \theta + 1}{\cos \theta_E + 1}. \quad (\text{S30})$$

For $\theta = 163.3^\circ$ and $\theta_E = 116.0^\circ$,⁷ φ is estimated to be $\varphi = 0.075$.

Finally, we estimate the net propulsion force F_n to be:

$$F_n = F_p - F_a = F_a = \sigma \cdot l(x) \cdot \alpha \cdot (\kappa_p - \kappa_a) = \sigma \cdot l(x) \cdot \alpha \cdot \left(\frac{\psi - \cos \psi \sin \psi}{2 \cdot \sin \psi} - 2 \cdot \cos \psi \cdot \frac{\varphi^{1/2}}{\pi^{1/2}} \right). \quad (\text{S31})$$

It should be noted that the necessary condition for the movement of the meniscus is that $\kappa_p - \kappa_a > 0$, which is the case for the explored opening angle range.

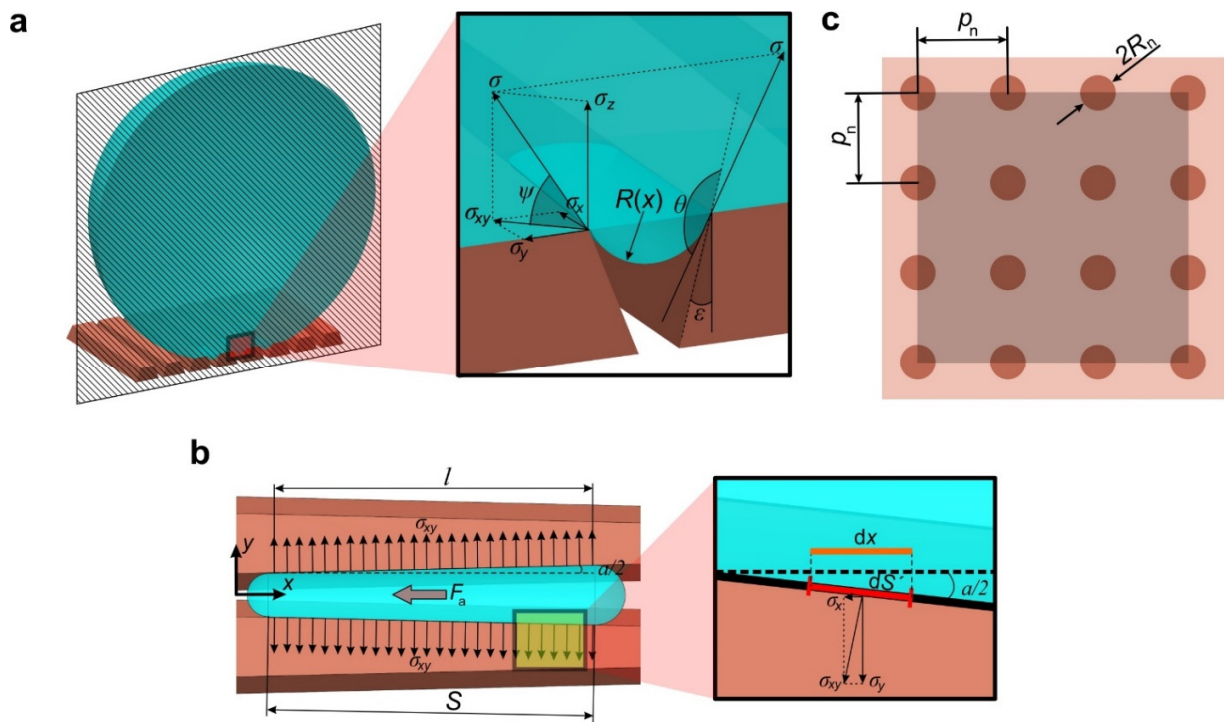


Figure S2. (a) Geometrical considerations and resolution of the adhesion force per unit length σ into its components along x , y and z directions. 3D view of the meniscus cross section. (b) Further geometrical considerations and force analysis on the meniscus, top view. (c) Approximation of nanostructure needles as an array of nanopillars with pitch p_n and diameter of nanopillar cross section $2R_n = 200\text{nm}$.

Discussion S2: Estimation of meniscus length l and parametric prediction of maximum net propulsion force F_n .

The length of the meniscus under the droplet, l , is needed to estimate the net propulsion force F_n . This length is obtained from geometrical considerations combined with experimental recordings of the droplet motion. We assume that the meniscus length can be approximated based on the observed diameter of the droplet contact disc l_d (Figure S3a), for every position x of the droplet centroid. Here, the contact disc for all opening angles is intermittent comprising interchanging regions of solid-water (ridge contact) and water-air (hanging meniscus) interfaces. After deposition of the droplet on the structured surface, oscillations are induced during the droplet motion caused by the detachment of the droplet from the tip of the capillary tube. These oscillations affect the contact disc, which oscillates as well. Due to viscous dissipation, these oscillations weaken with time. We believe that these oscillations do not affect the problem investigated since they show a specific increasing trend which is clear if we apply moving averaging fitting. Therefore, in order to highlight and more clearly show this oscillation-free increasing trend we fitted the experimental data with moving averaging curve fitting. Thus, for the estimation of the propulsion force and associated variables, we considered this fitting (Figure S3b).

With the help of the schematic depicted in Figure S3c the length of meniscus is considered to be the length of the trapezoidal segment of the droplet contact disc contained within the microtrack (Figure S3c):

$$l(x) = (OA) + (OB) \quad (S32)$$

Based on the geometrical considerations shown in Figure S3c the length of the meniscus is obtained by the following equation:

$$l(x) = \frac{\left(l_d^2 \cdot \left(1 + \tan^2 \frac{a}{2} \right) - \left(2 \tan \frac{a}{2} \cdot x + w_o \right)^2 \right)^{0.5}}{1 + \tan^2 \frac{a}{2}} \quad (S33)$$

Finally, with the help of equation S31, the net propulsion force F_n is given by the following equation:

$$F_n = \sigma \cdot \alpha \cdot \frac{\left(l_d^2 \cdot \left(1 + \tan^2 \frac{a}{2} \right) - \left(2 \tan \frac{a}{2} \cdot x + w_o \right)^2 \right)^{0.5}}{1 + \tan^2 \frac{a}{2}} \cdot \left(\frac{\psi - \cos \psi \sin \psi}{2 \cdot \sin \psi} - 2 \cdot \cos \psi \cdot \frac{\phi^{1/2}}{\pi^{1/2}} \right) \quad (S34)$$

Next, we use the above expression in order to obtain insights on the optimization of the droplet self-propulsion process. To this end, we explore whether F_n has a maximum at specific value of opening angle α . Since F_n increases monotonically with the position x of the droplet centroid, our parametric study is conducted at the end of the microtrack length. Based on experimental observations for the angles we studied and interpolation for other angles we did not explicitly investigate, we define a continuous fitting curve that enables the estimation of l_d (Figure S3d(i)). Our parametric study shows that indeed F_n features a maximum at a specific value of the opening angle, which depends on the length of the microtracks (Figure S3d(ii)). Note that such values are only approximate estimates and are meant to serve as a guide for the range of angle values that should yield sufficient droplet transport depending on application needs.

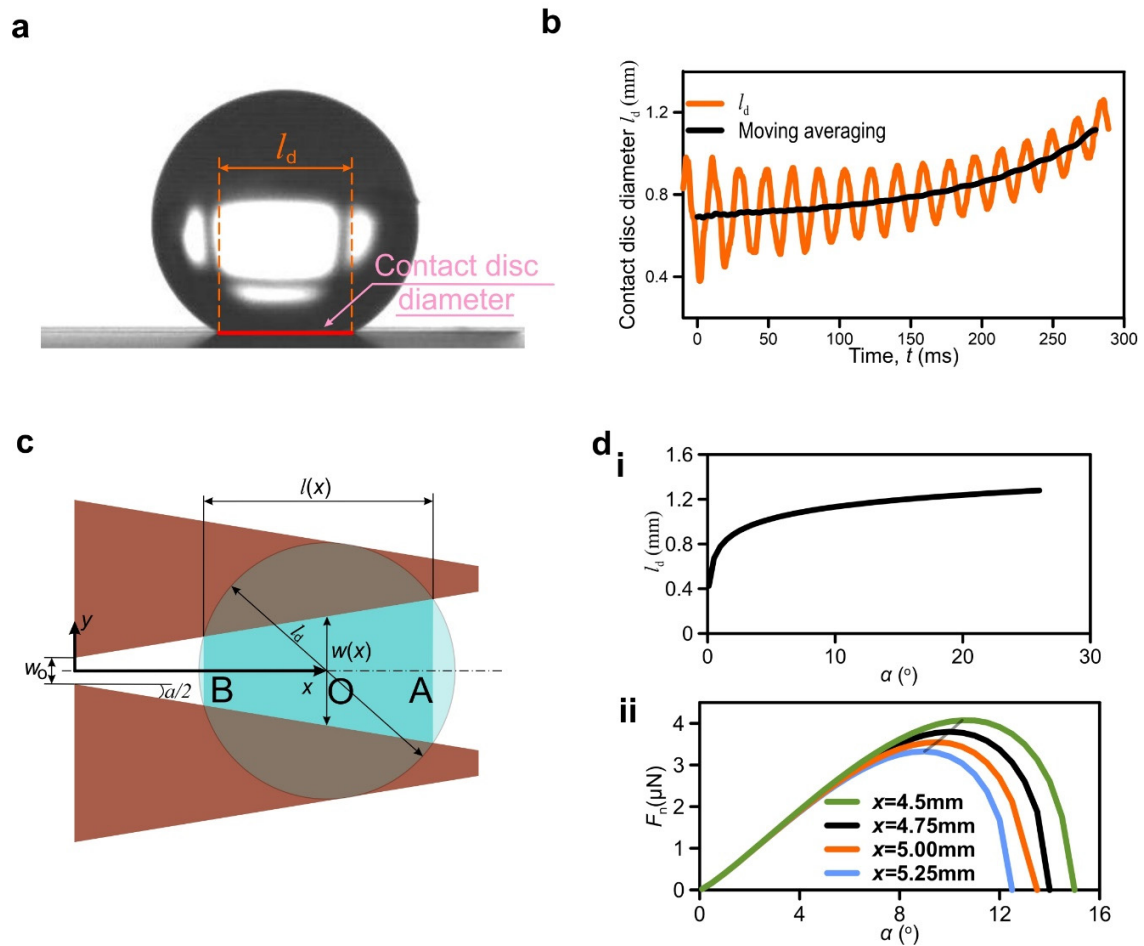


Figure S3. (a) Contact disc meniscus diameter l_d as can be observed from the video recordings. (b) Extracted contact disc diameter l_d versus time t for $\alpha = 9^\circ$. Curve is fitted with moving averaging using 19 measurement points. (c) Geometrical considerations of the estimation of the meniscus' length $l(x)$. (d) (i) Fitting curve for the estimation of the contact disc's diameter l_d . (ii) Net propulsion force F_n versus opening angle α for various lengths of microtracks or alternatively for various travelling distances.

Discussion S3: Estimation of total propulsion force $F_{n,\text{total}}$ for the case of multiple menisci formation.

Taking into consideration that $F_n \propto l$, for the case of the formation of multiple menisci, the calculation of the total net propulsion force $F_{n,\text{total}}$ is reduced to the calculation of the total length of the formed menisci altogether. As an example, we calculate the $F_{n,\text{total}}$ for the case of $\alpha=1^\circ$ where 5 menisci are formed. For the rest of the cases *i.e.* $\alpha=5,9^\circ$ only one meniscus is formed. Assuming that the projection of the bottom area of the droplet forms a circle of diameter l_d , the condition for the formation of m menisci is $(m-1)p < l_d < (m+1)p$. For the case of $\alpha=1^\circ$ it is $2p < \frac{l_d}{2} < 3p$ which means that indeed 5 menisci are formed. A schematic representation of the menisci is shown in Figure S4. The total length l_{total} is given by the following equation:

$$l_{\text{total}} = l + 2 \cdot l_p + 2 \cdot l_{2p} \quad (\text{S35})$$

where l_p and l_{2p} are the lengths of the menisci residing at distance p and $2p$ respectively from the centerline of the contact disc of the droplet (Figure S4). With the help of $\triangle OAB$ and $\triangle OCD$ we obtain the expressions :

$$l_p = \left(l_d^2 - (2p)^2 \right)^{\frac{1}{2}}, \text{ and} \quad (\text{S36})$$

$$l_{2p} = \left(l_d^2 - (4p)^2 \right)^{\frac{1}{2}}. \quad (\text{S37})$$

From the above,

$$l_{\text{total}} = l + 2 \cdot \left(l_d^2 - (2p)^2 \right)^{\frac{1}{2}} + 2 \cdot \left(l_d^2 - (4p)^2 \right)^{\frac{1}{2}}. \quad (\text{S38})$$

Combining equations S31 and S38 yields:

$$F_{n,\text{total}} = \sigma \cdot \left(l + 2 \cdot \left(l_d^2 - (2p)^2 \right)^{\frac{1}{2}} + 2 \cdot \left(l_d^2 - (4p)^2 \right)^{\frac{1}{2}} \right) \cdot \alpha \cdot (\kappa_p - \kappa_a). \quad (\text{S39})$$

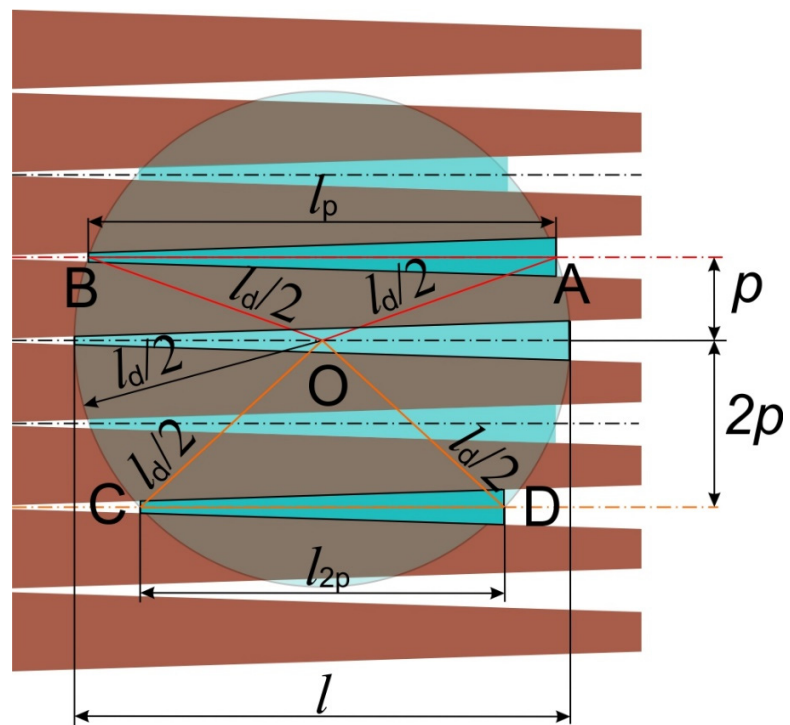


Figure S4. Geometrical notations for the calculation of the total net propulsion force $F_{n,\text{total}}$. The contact disc (teal color) is intermittent comprising interchanging solid-water contact segments and menisci with radius $l_d/2$.

Discussion S4: Estimation of critical tilt angle β_{cr}

In this section, we perform a force balance on the droplet as it is formed and is released from a capillary tip inside a microchannel, including the case where the droplet is released in a tilted channel, which generates an additional component of the gravitational force, resisting the droplet release. The analysis includes also the capillary force at the needle tip releasing the droplet, which acts before droplet release. Note to this end, that in experiments this force can be easily eliminated with a quick withdrawal of the needle causing droplet separation. However, for the sake of generality, we included it in the model as well and obtain result with and without its presence. The calculation of the critical tilt angle β_{cr} , defined as the tilt angle above which the droplet fails to detach from the tip of the capillary tube, starts with the following force balance (Figure S5a):

$$F_{a,tip} + 2 \cdot F_{a,cd} + F_{g,x} = 2 \cdot F_n \quad (S40)$$

where $F_{a,tip}$ is the pinning force exerted on the droplet, originating from the tip of the capillary tube, $F_{a,cd}$ is the adhesion force due to the surface tension of the liquid and associated with the contact disc, $F_{g,x}$ is the x -component of the droplet's gravitational force and F_n is the net propulsion force coming from the formed menisci of each of the structured walls of the channel. When $2 \cdot F_n$ overcomes the total resisting force, ejection occurs. First, it is necessary to estimate $F_{a,tip}$ based on Video S4 at which $\beta = 0^\circ$ (Figure S5b). We estimate the volume of the ejected droplet to be $\Omega = 110\text{nl}$ based on the acquired video frames of the droplet moving along the superhydrophobic planar surfaces and assuming that the droplet forms a spherical cap. Then based on the geometrical considerations of the droplet shape at ejection, l_d is calculated. The total volume of the droplet is given by the following equation (Figure S5b):

$$\Omega = 2 \cdot \Omega_m + \Omega_p, \quad (S41)$$

where Ω_p is the volume of the formed water "pancake" due to the squeezing of the droplet and Ω_m is the volume of the formed meniscus. Assuming that the pancake is a disc of diameter l_d and thickness h , its volume is given by the following equation:

$$\Omega_p = \pi \left(\frac{l_d}{2} \right)^2 h. \quad (\text{S42})$$

With the help of equation S15 the volume of each meniscus is calculated by the integral:

$$\Omega_m = \int_{x_{\text{tip}}}^{x_{\text{tip}}+l} d\Omega'' = \frac{(2 \tan \frac{\alpha}{2} \cdot x + w_o)^2}{4 \sin^2 \psi} (\psi - \cos \psi \sin \psi) dx \quad (\text{S43})$$

which finally yields:

$$\Omega_m = \frac{2\pi \sin \psi}{3 \tan \frac{\alpha}{2}} \left[\left(\frac{2 \tan \frac{\alpha}{2} (x_{\text{tip}} + l) + w_o}{2 \sin \psi} \right)^3 - \left(\frac{2 \tan \frac{\alpha}{2} x_{\text{tip}} + w_o}{2 \sin \psi} \right)^3 \right] (\psi - \cos \psi \sin \psi). \quad (\text{S44})$$

For the calculation of l included in the previous equation S44 we use equation S33:

$$l(x_{\text{tip}} + \frac{l_d}{2}) = \frac{\left(l_d^2 \cdot \left(1 + \tan^2 \frac{\alpha}{2} \right) - \left(2 \tan \frac{\alpha}{2} \cdot (x_{\text{tip}} + \frac{l_d}{2}) + w_o \right)^2 \right)^{0.5}}{1 + \tan^2 \frac{\alpha}{2}}. \quad (\text{S45})$$

The combination of equations S41, S42, S44 and S45 yields an expression of the volume Ω with l_d the unknown variable:

$$\Omega = 2 \cdot \frac{2\pi \sin \psi}{3 \tan \frac{\alpha}{2}} \left[\left(\frac{2 \tan \frac{\alpha}{2} \left(x_{\text{tip}} + \frac{\left(l_d^2 \cdot \left(1 + \tan^2 \frac{\alpha}{2} \right) - \left(2 \tan \frac{\alpha}{2} \cdot \left(x_{\text{tip}} + \frac{l_d}{2} \right) + w_o \right)^2 \right)^{0.5}}{1 + \tan^2 \frac{\alpha}{2}} \right) + w_o}{2 \sin \psi} \right)^3 - \left(\frac{2 \tan \frac{\alpha}{2} x_{\text{tip}} + w_o}{2 \sin \psi} \right)^3 \right] \cdot (\psi - \cos \psi \sin \psi) + \pi \left(\frac{l_d}{2} \right)^2 h \quad (\text{S46})$$

Solving equation S46 computationally, we obtain $l_d = 0.76 \text{ mm}$. Knowing l_d , allows the calculation of the net propulsion force F_n . Force F_n is given by equation S34 and $F_{\text{a.cd}}$ is calculated by the following:

$$F_{\text{a.cd}} = \kappa_\phi \cdot l_d \cdot \sigma \cdot \xi \cdot (\cos \theta_{\text{rec}} - \cos \theta_{\text{adv}}), \quad (\text{S47})$$

where we introduce κ_ϕ owing to the fact the contact line is in contact with the features of the roughness topography that emerge at the surface.^{4,8} We also introduce a prefactor ξ that accounts for the actual deviation from the macroscopically measured dynamic contact angles *i.e.* the θ_{rec} and θ_{adv} , occurring due to the change (decrease) of the droplet size.⁹⁻¹¹ Therefore, in order to be able to obtain $F_{\text{a.cd}}$ the estimation of ξ is necessary. To estimate ξ we are using the acquired video frames of the droplet travelling along the planar superhydrophobic surfaces of the microchannel (Figure S5c). The motion of the droplet is described by the following equation:

$$\rho \cdot \Omega \cdot \gamma = F_v + F_{\text{a.cd}} \quad (\text{S48})$$

where ρ is the density of water, γ is the droplet deceleration and F_v is the viscous force. The deceleration of the droplet is calculated based on the velocity *versus* time data extracted by post processing of video S4 (Figure S5d). The velocity shows a linear dependence of time which means that the deceleration remains constant during the travel of the droplet at the value of $\gamma = 2.032 \text{ m} \cdot \text{s}^{-2}$. The viscous force F_v originates from the velocity gradients in the droplet

caused by shear at the liquid-solid interface of the contact disc. Thus, the wall shear stress τ_w at the liquid-solid interface of the contact disc is estimated based on the equation:

$$\tau_w = \mu \nabla u |_{y=0}, \quad (\text{S49})$$

where μ is the dynamic viscosity of water. With the assumption that the viscous dissipation occurs mainly within a volume contained between the contact disc and the center of the spherical-cap-like droplet¹² and that the velocity distribution in this region resembles a Couette flow^{4,12-14} we can obtain an expression of the velocity gradient :

$$\nabla u \sim V / l_c = \nabla u |_{y=0}. \quad (\text{S50})$$

where l_c is the vertical distance of the center of the spherical-cap-like surface from the contact disc of diameter $l_{d,\text{drop}}$. Based on the geometrical considerations shown in Figure S5c

$$l_c = \frac{l_{d,\text{drop}}}{2} \tan(\theta - \pi / 2) \quad (\text{S51})$$

Finally, combining equations S48, S49, S50 and S51 the viscous force F_v is estimated as follows:

$$F_v = \varphi \pi \left(\frac{l_{d,\text{drop}}}{2} \right)^2 \mu \frac{V}{\frac{l_{d,\text{drop}}}{2} \tan(\theta - \pi / 2)}. \quad (\text{S52})$$

With the help of equations S47, S48 and S52 we obtain an expression for the prefactor ξ :

$$\xi = \left(\rho \cdot \Omega \cdot \gamma - \varphi \pi \left(\frac{l_{d,\text{drop}}}{2} \right)^2 \mu \frac{V}{\frac{l_{d,\text{drop}}}{2} \tan(\theta - \pi / 2)} \right) / \left(\kappa_\varphi \cdot l_{d,\text{drop}} \cdot \sigma \cdot (\cos \theta_{\text{rec}} - \cos \theta_{\text{adv}}) \right). \quad (\text{S53})$$

The estimation of ξ which has the value of 4.2, allows us the calculation of $F_{a,tip}$ as well as the ratio between the viscous and the adhesion forces $\frac{F_v}{F_{a,tip}}$ which is 0.9% . This denotes that F_v is negligible compared to the $F_{a,tip}$. It should be noted that the calculated values are based on the analysis of video S4.

Returning to equation S40 and since forces $F_{a,cd}$, $F_{g,x}$ and F_n can now be determined, we can calculate the pinning force $F_{a,tip}$ for $\beta = 0^\circ$ ($F_{g,x} = 0$). Finally, assuming that the $F_{a,tip}$ remains the same irrespectively of the droplet size and tilt angle β , we can now determine for every $\beta > 0$ the ejected droplet size, using again equation S40. For this we use the force balance shown in S5a with unknown variables β and l_d . Consequently, S40 becomes:

$$F_{a,tip} + 2 \cdot F_{a,cd}(l_d) + \rho \cdot \Omega(l_d) \cdot g \cdot \sin \beta - 2 \cdot F_n(l_d) = 0 . \quad (S54)$$

Our model suggests that since we are able to minimize the adhesion force $F_{a,cd}$ due to surface tension by reaching extreme water repellency, maximize the net propulsion force F_n since we are using an opening angle of $\alpha = 9^\circ$ (see Discussion S2), the force that needs to be regulated in order to achieve larger tilt angles β and smaller ejected volumes Ω is $F_{a,tip}$. Therefore, by changing the size and the wetting properties of the capillary tube used, minimization of $F_{a,tip}$ can be achieved. It can even be nullified by introducing a mechanism where the capillary tube is rapidly removed from the deposited droplet. Therefore, we calculated the volume ejected for different magnitudes meaning for $2/3F_{a,tip}$, $1/3F_{a,tip}$ and $F_{a,tip} = 0$. The tilt angle β versus ejected volume Ω is shown in Figure S5e. By computing β_{cr} for each case we are able to draw a line with the help of which we can define a region where no ejection is possible. The graph suggests that for the capillary tube used, for tilt angle $\beta > \beta_{cr} \approx 23^\circ$ a droplet fails to eject and it is not possible to eject droplets with volumes $\Omega > 325nl$. On the other hand, by nullifying $F_{a,tip}$, the critical tilt angle becomes $\beta_{cr} = 90^\circ$ enabling ejection of tiny droplets down to $13nl$.

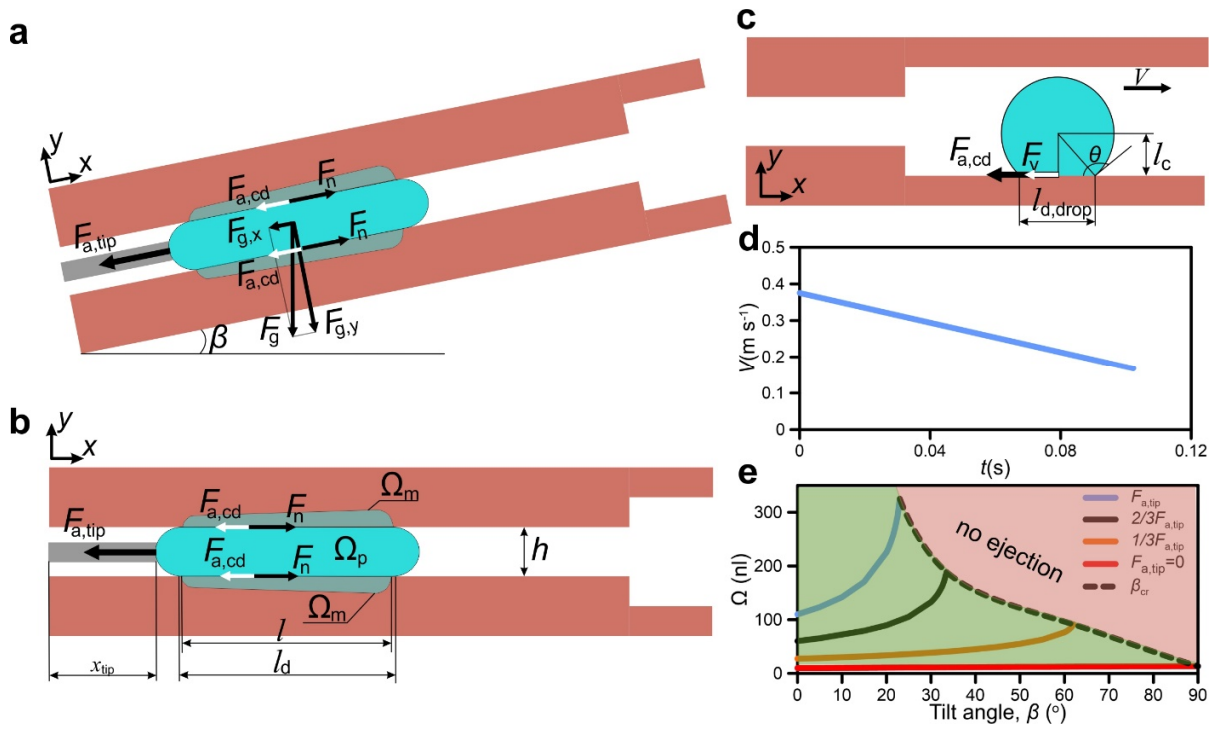


Figure S5. Force balance on a droplet in microchannel while being pinned on the capillary tube's tip and while growing for (a) $\beta = 0^\circ$ and (b) $\beta > 0^\circ$. (c) Force balance on a droplet entering the planar superhydrophobic section of the microchannel. (d) Droplet velocity V versus time t along the planar superhydrophobic section of the microchannel. (e) Ejected droplet volume Ω versus tilt angle β of the microchannel.

Discussion S5: Laser micromachining

The fabrication of lateral gradients has been carried out by ultra-short pulsed laser ablation generating a distinct surface morphology on the copper substrates.¹⁵ A frequency-doubled Amphos 200 laser source with 515nm wavelength, 800fs pulse duration, average power up to 120W and a tunable repetition rate is coupled *via* modifying wave plate into a galvo scanner mounted on the z-axis, shown in Figure S6a. The polarization state at the focal plane is circular by wave plates ($\lambda/2$ and $\lambda/4$), thus reducing a directional ablation on the copper substrates and possible induced ripple structures (Laser-Induced Periodic Surface Structures, LIPSS). The positioning of the specimen with precision at the x and y axes enables stitching to overcome the limitation of the field of view (FOV) with length l_{FOV} in Figure S6b. A galvo scanner with fast dielectric mirrors and a telecentric f-theta lens with focal length of 163mm leads to a laser spot diameter of $18\mu\text{m}$ with the used configuration. To reach a certain structural depth with high precision the laser ablation strategy is crucial and a layer by layer approach is used, depicted in Figure S6c. The laser beam moves over the surface leading to ablation in parallel lines with a distance of l_b and switched on and off at the locations to be removed. An acceleration path of length d_{sky} avoids effects of non-constant beam velocity that could possibly change the ablation condition. Additionally, each layer is rotated by an angle γ_{Layer} mitigating the accumulation of errors by superposition of ablation grooves from the previous removed layer. A parametric study on copper reveals the ablation behavior and point to a certain layer thickness and surface quality. This allows computation

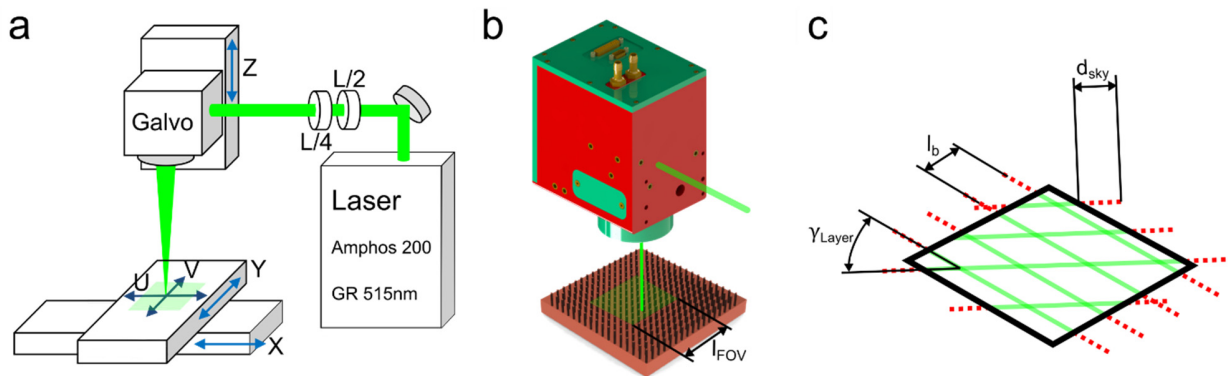


Figure S6. Laser ablation tool configuration including source, beam guidance with wave plates, and axes **(a)**. Fast optical axes (UV) of a galvo scanner enable a high surface speed within the field of view with length l_{FOV} **(b)**. The orthogonal beam incidence needs a strategy to mitigate errors overlapping the laser with l_b and rotating each layer by an angle γ_{Layer} **(c)**. Example of covering a square geometry the galvo mirror accelerates with the laser off (red dotted) and turning it on (green) after a length d_{sky} reaching constant velocity.

of the laser ablation paths with the designed geometry generating the numerical machine code to control the laser ablation tool.¹⁶

To laser manufacture the microtracks the laser was set to an average power of 2W at 1MHz repetition rate. Moving the pulsed laser radiation with 2 μ m step at 0.5 m s⁻¹ surface speed leads to an ablated layer thickness of 3.6 μ m. Next, the structures are laser machined starting by removing two layers with 90° rotation. Then, the microtracks are generated by ablation of 90 or 67 layers rotated by 23° each. This produces the defined structure with a surface roughness $R_a < 1\mu$ m and a structural depth of 330 μ m or 240 μ m respectively.

Discussion S6: Surface characterization

The surface morphology was examined using Scanning Electron Microscopy (SEM) as well as an optical microscope. Figure S7 shows the copper-based microtracks for opening angles $\alpha = 1^\circ$ (Figure S7a), $\alpha = 5^\circ$ (Figure S7b) and $\alpha = 9^\circ$ (Figure S7c). We also employ Energy Dispersive X-ray Spectroscopy (EDX) for the chemical analysis of the fabricated surfaces. The laser-micromachined surface for an opening angle of $\alpha = 1^\circ$ is shown in Figure S8a. We acquire SEM pictures at the beginning, middle and the end of the microstructured surface (Figure S8a(i)). The SEM pictures in Figure S8a(ii) show the precise surface architecture. Next step is the characterization of these laser-machined microstructures superimposed with the clustered nanoneedles. SEM pictures in Figure S8b show different magnifications of the clustered nanoneedles covering the microtracks and microgrooves at the beginning (Figure S8b(i)) and the middle (Figure S8b(ii)) of the laser machined surface. It is worth saying that the cluster of nanoneedles cover uniformly not only planar regions such as those of the microtracks, but also their sidewalls as well as the bottom of the microgrooves. This highlights the value of the wet chemistry etching, which accommodates the nanostructuring of 3D geometries.

Implementing accelerating voltage of 10kV, EDX analysis on the laser micromachined surface (after cleaning) indicates only a strong signal corresponding to copper (Cu) as shown in Figure S8c (red dashed line). The analysis of the final surface (Figure S8c, black solid line) shows a peak of (Cu), and three distinctive signals of (C), (F) and (S) indicating the presence of the perfluorodecanethiol coating. Moreover, a signal of oxygen (O) is attributed to the etching process and the growth of $\text{Cu}(\text{OH})_2$ nanoneedles. It should be noted that plots are normalized by the maximum of the Counts Per Second *i.e.* CPS_{max} that correspond to the peak of Cu for the case of the laser micromachined surface and to the peak of F for the case of the superhydrophobic microtracks.

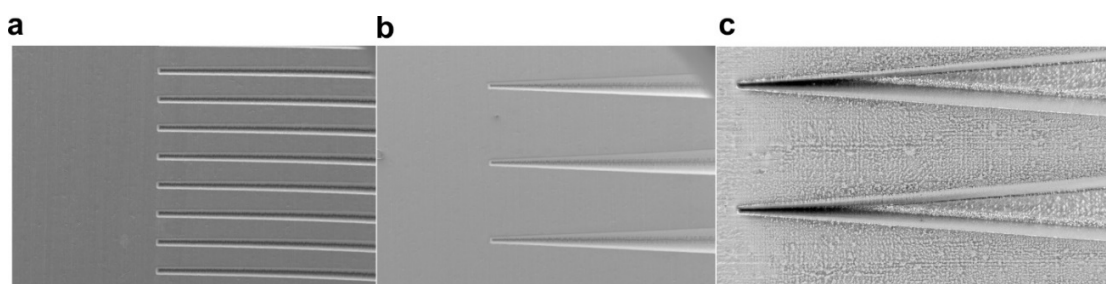


Figure S7. Microscope pictures of the microtracks with opening angles: **(a)** $\alpha = 1^\circ$ (SEM), **(b)** $\alpha = 5^\circ$ (SEM), and **(c)** $\alpha = 9^\circ$ (optical microscopy).

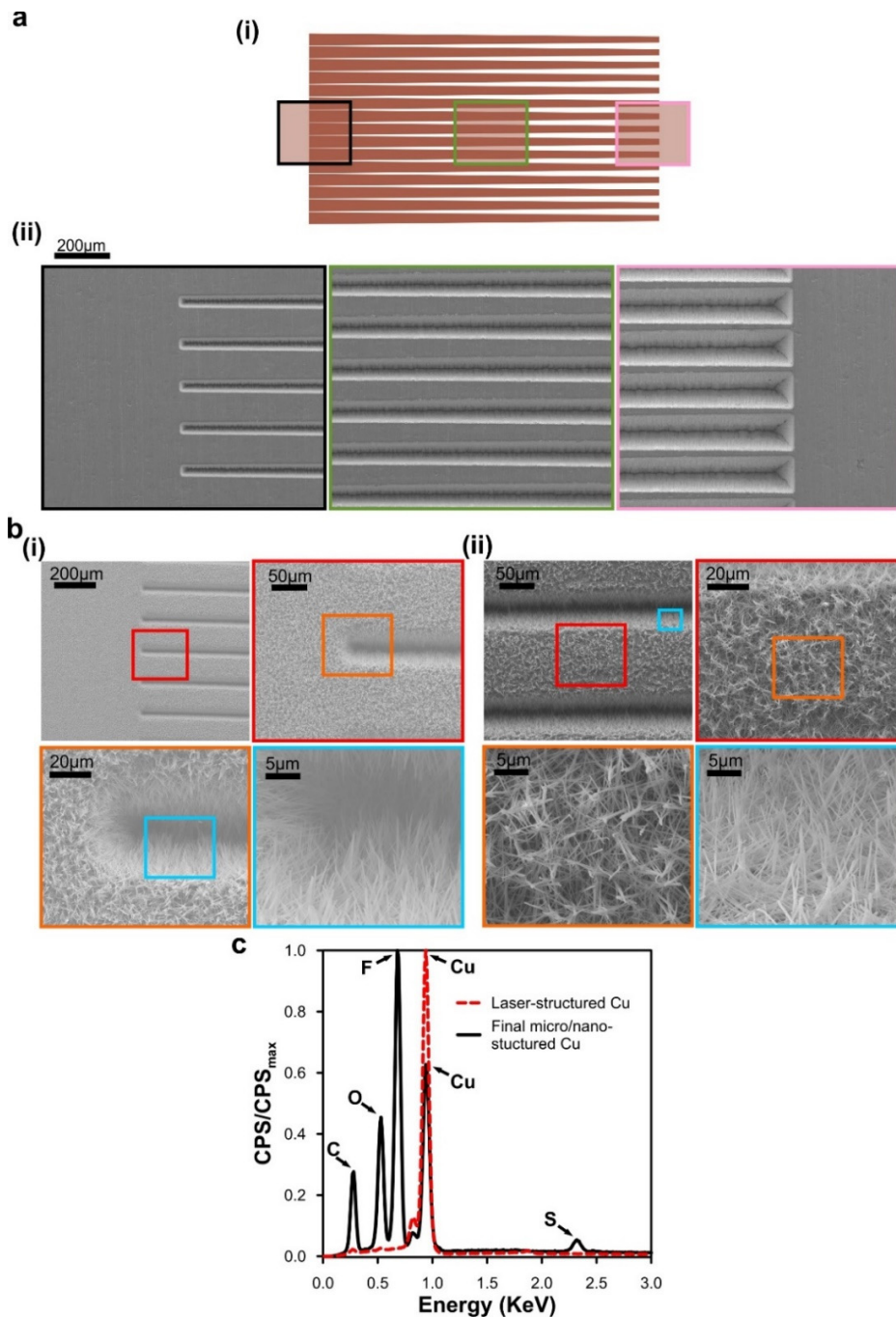


Figure S8. (a) (i) Schematic illustration and (ii) SEM pictures acquired at the beginning, middle and end of the laser micromachined backgammon-like surfaces. A surface with opening angle $\alpha = 1^\circ$ is shown. (b) Laser micromachined surface superimposed with clustered nanoneedles. SEM pictures of different magnification are shown that correspond to the beginning (i) and middle (ii) of the backgammon-like surface. (c) EDX analysis of the laser-micromachined surface after cleaning (dashed red line) and the final micro/nano structured superhydrophobic surface.

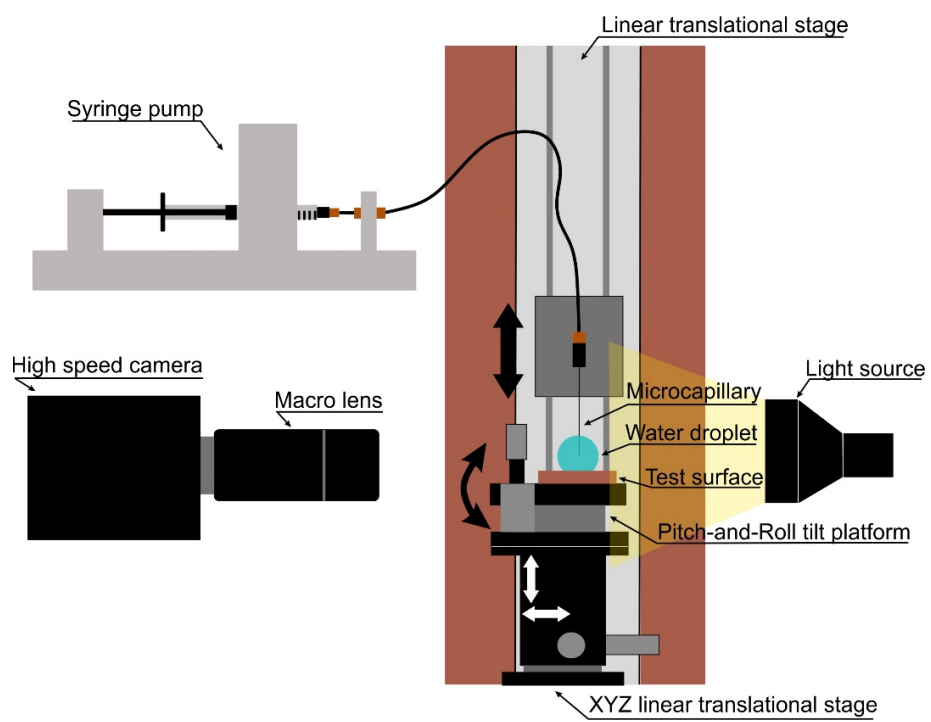


Figure S9. Schematic of the experimental setup.

Table S1. Summary of the geometrical parameters used of each of the tested surface

	Opening angle (°), α	Pitch (μm), p	Length (mm) , L	Depth (μm), d
Surface #1	1	150	5.25	240
Surface #2	5	500	5.25	330
Surface #3	9	880	5.25	330

Supporting videos

Video S1. Droplet self-propulsion on the three microtrack surfaces with opening angle $\alpha = 1, 5, 9^\circ$. Recording frame rate 1000fps. Playback speed $\times 1/30$. Scale bars correspond to 1mm.

Video S2. Drop impact on a microtrack surface with opening angle $\alpha = 9^\circ$. Recording frame rate 1000fps. Playback speed $\times 1/100$. Scale bar corresponds to 1mm.

Video S3. Mixing of two droplets with the assistance of microtracks with opening angle $\alpha = 9^\circ$. Recording frame rate 1000fps. Playback speed $\times 1/30$. Scale bar corresponds to 2mm.

Video S4. Ejection and movement of droplet inside a microchannel (tilt angle $\beta = 0^\circ$), the walls of which consist of microtracks with opening angle $\alpha = 9^\circ$. Recording frame rate 8000fps. Playback speed $\times 1/260$. Scale bar corresponds to 5mm.

Video S5. Ejection and movement of droplet inside a tilted microchannel (tilt angle $\beta = 10^\circ$) the walls of which consist of microtracks with opening angle $\alpha = 9^\circ$. Recording frame rate 8000fps. Playback speed $\times 1/260$. Scale bar corresponds to 5mm.

References

- (1) Metz, T.; Paust, N.; Zengerle, R.; Koltay, P. Capillary Driven Movement of Gas Bubbles in Tapered Structures. *Microfluid. Nanofluidics* **2010**, *9*, 341–355.
- (2) Renvoisé, P.; Bush, J. W. M.; Prakash, M.; Quéré, D. Drop Propulsion in Tapered Tubes. *Europhys. Lett.* **2009**, *86*, 64003.
- (3) Sharma, C. S.; Stamatopoulos, C.; Suter, R.; Von Rohr, P. R.; Poulikakos, D. Rationally 3D-Textured Copper Surfaces for Laplace Pressure Imbalance-Induced Enhancement in Dropwise Condensation. *ACS Appl. Mater. Interfaces* **2018**, *10*, 29127–29135.
- (4) Smith, J. D.; Dhiman, R.; Anand, S.; Reza-Garduno, E.; Cohen, R. E.; McKinley, G. H.; Varanasi, K. K. Droplet Mobility on Lubricant-Impregnated Surfaces. *Soft Matter* **2013**, *9*, 1772–1780.
- (5) Quéré, D. Wetting and Roughness. *Annu. Rev. Mater. Res.* **2008**, *38*, 71-79.
- (6) Quéré, D. Non-Sticking Drops. *Reports Prog. Phys.* **2005**, *68*, 2495–2532.
- (7) Patois, T.; Et Taouil, A.; Lallemand, F.; Carpentier, L.; Roizard, X.; Hihn, J. Y.; Bondeau-Patissier, V.; Mekhalif, Z. Microtribological and Corrosion Behaviors of 1H,1H,2H,2H-Perfluorodecanethiol Self-Assembled Films on Copper Surfaces. *Surf. Coatings Technol.* **2010**, *205*, 2511–2517.
- (8) Yilbas, B. S.; Al-Sharafi, A.; Ali, H.; Al-Aqeeli, N. Dynamics of a Water Droplet on a Hydrophobic Inclined Surface: Influence of Droplet Size and Surface Inclination Angle on Droplet Rolling. *RSC Adv.* **2017**, *7*, 48806–48818.
- (9) Style, R. W.; Che, Y.; Park, S. J.; Weon, B. M.; Je, J. H.; Hyland, C.; German, G. K.; Power, M. P.; Wilen, L. a; Wettlaufer, J. S.; Dufresne, E. R. *Proc. Natl. Acad. Sci. U. S. A.* **2013**, *110*, 12541–12544.
- (10) Taylor, M.; Urquhart, A. J.; Zelzer, M.; Davies, M. C.; Alexander, M. R. Picoliter Water Contact Angle Measurement on Polymers. *Langmuir* **2007**, *23*, 6875–6878.
- (11) Huhtamäki, T.; Tian, X.; Korhonen, J. T.; Ras, R. H. A. Surface-Wetting Characterization Using Contact-Angle Measurements. *Nat. Protoc.* **2018**, *13*, 1521–1538.
- (12) Moradi, N.; Varnik, F.; Steinbach, I. Contact Angle Dependence of the Velocity of Sliding Cylindrical Drop on Flat Substrates. *Epl* **2011**, *95*.
- (13) Stamatopoulos, C.; Schutzius, T. M.; Köppl, C. J.; Hayek, N. El; Maitra, T.; Hemrle, J.; Poulikakos, D. On the Shedding of Impaled Droplets: The Role of Transient Intervening Layers. *Sci. Rep.* **2016**, *6*, 1-9.
- (14) Smith, A. F. W.; Mahelona, K.; Hendy, S. C. Rolling and Slipping of Droplets on Superhydrophobic Surfaces. *Phys. Rev. E* **2018**, *98*, 1–8.
- (15) Ackerl, N.; Wegener, K. Ablation Characteristics of Alumina and Zirconia Ceramics on Ultra-Short Pulsed Laser Machining. *J. Laser Micro/Nanoengineering* **2019**, *14*.
- (16) Ackerl, N.; Warhanek, M.; Gysel, J.; Wegener, K. Path Calculation of 7-Axes Synchronous Quasi-Tangential Laser Manufacturing. *Int. J. Adv. Manuf. Technol.* **2019**, *103*, 1105–1116.